

# Gyrokinetic simulations of zonal flows and ion temperature gradient turbulence in HL-2A ITB plasmas

Cite as: Phys. Plasmas **29**, 012508 (2022); <https://doi.org/10.1063/5.0070354>

Submitted: 06 September 2021 • Accepted: 05 January 2022 • Published Online: 25 January 2022

 J. Q. Xu, X. D. Peng, G. Z. Hao, et al.



[View Online](#)



[Export Citation](#)



[CrossMark](#)

Physics of Plasmas

Papers from 62nd Annual Meeting of the  
APS Division of Plasma Physics

[Read now!](#)



# Gyrokinetic simulations of zonal flows and ion temperature gradient turbulence in HL-2A ITB plasmas

Cite as: Phys. Plasmas **29**, 012508 (2022); doi: 10.1063/5.0070354

Submitted: 6 September 2021 · Accepted: 5 January 2022 ·

Published Online: 25 January 2022



View Online



Export Citation



CrossMark

J. Q. Xu,<sup>1</sup> X. D. Peng,<sup>1,a)</sup> G. Z. Hao,<sup>1</sup> W. Chen,<sup>1</sup> J. Q. Li,<sup>1</sup> H. P. Qu,<sup>1</sup> J. C. Li,<sup>2</sup> G. Z. Ren,<sup>1,3</sup> X. X. He,<sup>1</sup> and Y. G. Li<sup>1</sup>

## AFFILIATIONS

<sup>1</sup>Southwestern Institute of Physics, Chengdu 610041, People's Republic of China

<sup>2</sup>Department of Earth and Space Sciences, Southern University of Science and Technology, Shenzhen 518055, Guangdong, People's Republic of China

<sup>3</sup>School of Physics, Dalian University of Technology, Dalian 116024, People's Republic of China

<sup>a)</sup>Author to whom correspondence should be addressed: pengxd@swip.ac.cn

## ABSTRACT

The characteristics of zonal flows (ZFs) in ion temperature gradient (ITG) turbulence during the formation of internal transport barrier (ITB) have been investigated by nonlinear gyrokinetic simulations for the HL-2A tokamak experiment. The turbulent ion heat transport and zonal flow dynamics are investigated in the local turbulence limit for a neutral beam heated L-mode plasma. Linear stability analyses have shown that the maximum growth rate,  $\gamma^{\max}$ , is decreased across the whole confinement region during the formation of ITB although the critical parameter,  $\eta_i$ , is increased, which is identified to be due to the stabilizing of ITG with an increased ion-to-electron temperature ratio  $\tau$ . The entropy generated by ion heat flux is significantly decreased together with the enhanced ZF amplitude and reduced ion heat transport when ITB has been fully developed, especially the modes with intermediate radial wavenumbers, implying that the long and medium radial scale turbulences are strongly suppressed by the ZF shear. Meanwhile, the long-range correlation and relative energy of the self-generated ZF are increased while the turbulent energy is decreased when ITB is triggered, indicating that the ZF gains more energy from background turbulence. It is found that the ratio between  $\tau$  and  $\eta_i$  is a key parameter in determining the ZF shearing rate  $\omega_{E \times B}^{ZF}$  and  $\gamma^{\max}$ . The value of  $\omega_{E \times B}^{ZF} > \gamma^{\max}$  occurs around  $\tau/\eta_i > 1.4$ , which is suggested to be responsible for the reduction of ion heat transport and hence the ITB formation.

Published under an exclusive license by AIP Publishing. <https://doi.org/10.1063/5.0070354>

## I. INTRODUCTION

Turbulent transport in magnetically confined devices has a direct impact on the performance of confinement for fusion devices, which makes it a critical issue. In general, neoclassical theories cannot explain the experimentally observed cross field transport in tokamaks, where the latter is usually up to two orders of magnitude than the neoclassical prediction,<sup>1</sup> which is generally recognized to be due to the anomalous transport induced by various kinds of temperature gradient-driven microinstabilities.<sup>2</sup> Theories and experiments both indicate that the tokamak plasma is a highly complex system involving multi-scale instability modes, among whom the anomalous transport is basically characterized by three different types of microinstabilities, namely, the large-scale ( $k_\theta \rho_i \approx 0.1-0.5$ ) ion temperature gradient (ITG) mode,<sup>3</sup> the medium-sized ( $k_\theta \rho_i \approx 0.5-2$ ) trapped electron mode (TEM),<sup>4</sup> and the short wavelength ( $k_\theta \rho_i \geq 2$ ) electron temperature gradient (ETG)

mode,<sup>5</sup> which are held responsible for ion heat transport, electron particle/heat transport, and electron heat transport, respectively. Here,  $k_\theta$  is the poloidal wave number and  $\rho_i$  is the ion gyroradius. It is obvious that the stability of these modes depends on various plasma parameters, including  $\mathbf{E} \times \mathbf{B}$  shear flows,<sup>6</sup> magnetic shear,<sup>7</sup> Shafranov shift,<sup>8</sup> ion-to-electron temperature ratio,<sup>9</sup> and impurity/charge concentration.<sup>10</sup> Since these parameters act differently on the different wavelength scales of the turbulent modes, their influence on the respective transport channels also varies.

Aiming to improve the confinement since the first observation of the H mode,<sup>11</sup> various kinds of improved confinement scenarios have been observed in tokamaks and helical devices. The occurrence of internal transport barriers (ITBs), characterized by a steep gradient formation in temperature profiles and a decrease in the thermal diffusivity in the plasma core region has obvious advantages in increasing

the energy confinement.<sup>12–14</sup> The turbulent ion heat transport in ITBs is thought to be dominated by ITG modes that are destabilized when the ion temperature gradient exceeds a critical value  $R/L_{T_i|crit}$ ,<sup>9</sup> whose stability depends on the ratio of  $T_i/T_e$  as well and an increasing value of  $T_i/T_e$  will stabilize the modes and shift the critical  $R/L_{T_i|crit}$  to smaller values as a consequence of the quasi-neutrality condition.<sup>15</sup> This is in consistent with most present day ITB experiments, which are usually performed at low density, i.e., weakly coupled ions and electrons, and easily assisted in the plasma core where the magnetic shear is low or negative and  $T_i \gg T_e$  by heating ions through the method of neutral beam injection (NBI), including tokamaks,<sup>16–18</sup> stellarators<sup>19–21</sup> and reversed field pinch plasmas.<sup>22</sup> In these experiments, the NBI not only acts as the dominant heating source, but also plays a decisive role in the suppression of the ITG turbulence.

At present, it is widely known that the cause of the decrease in ion heat transport in ITBs is ascribed to the relationship between  $\mathbf{E} \times \mathbf{B}$  shear flow and turbulence. The role of the  $\mathbf{E} \times \mathbf{B}$  shear flow has also been confirmed in the experiment on many tokamaks, such as TFTR,<sup>23</sup> JET,<sup>24</sup> DIII-D,<sup>25</sup> and JT-60U.<sup>26</sup> The  $\mathbf{E} \times \mathbf{B}$  shearing rate ( $\omega_{E \times B}$ ) was found to be close to the linear growth rate of the ITG modes ( $\gamma_{lin}$ ) at the time of barrier formation when compared with several tokamaks.<sup>27</sup> For instance, an analysis of the DIII-D discharge has shown that  $\omega_{E \times B} > \gamma_{lin}$  holds across the whole plasma.<sup>28</sup> Once the ITB is triggered, both the  $\mathbf{E} \times \mathbf{B}$  shear flow and pressure gradients are simultaneously increased with the condition that  $\omega_{E \times B} > \gamma_{lin}$ . Although there are much literature about the relationship between the  $\mathbf{E} \times \mathbf{B}$  shear flow and the turbulence for the ITB plasma,<sup>29</sup> there are a few reports on the role of the zonal flows (ZFs)<sup>30</sup> on turbulence suppression and ITB formation. The relationship between the amplitudes of zero-frequency ZF and turbulence has been first investigated in ITB plasmas in the CHS device using dual heavy ion beam probe (HIBP), showing that the turbulence amplitude is much lower and the magnitude of the ZF is larger in the plasma with ITB compared to that without it.<sup>31</sup> This result clearly shows the important role of ZF on the suppression of the turbulence and formation of the ITB. The ITB discharges usually have the feature of an increase in both the ion temperature gradient parameter  $\eta_i$  ( $\eta_i = L_n/L_{T_i}$ , where  $L_n$  and  $L_{T_i}$  are the scale lengths of density and ion temperature gradients, respectively) and ion-to-electron temperature ratio  $\tau$ , which is also the typical feature of ITB discharges in the HL-2A tokamak experiments.<sup>32</sup> Linear global gyrokinetic simulations utilizing gyrokinetic (GK) code that of GK-quasi-neutrality condition (GKNET) have also proved that the ITG with normalized wavenumber  $k_\theta \rho_i < 1$  is the dominating microinstability in ITB discharges, whereas TEM and a drift instability which show the hybrid characteristics between ITG and TEM take over when ITB collapses after ECRH on HL-2A.<sup>33</sup> Nevertheless, the effect of ZFs and the temperature ratio on heat transport and confinement have not been systematically investigated, which should be performed by nonlinear simulations. From this prospective, it is strongly suggested that turbulence in transport barriers is determined by the competition between the suppression of turbulence by the self-generated ZFs and the driving of ITG turbulence by an increased ion temperature gradient, which might be characterized by the parameter  $\tau/\eta_i$ . However, the effect of ion-to-electron temperature ratio and ion temperature gradient on the properties of self-generated zonal flow and its shearing rate still remains unclear, particularly the dynamics of different spatial scales of turbulence during the process of ITB formation. This paper is aimed at

providing an intuitive interpretation of these effects through nonlinear simulations, which is beneficial for the explanation of trigger and controlling mechanism of internal transport barriers.

The remainder of this paper is organized as follows. The theoretical model used in the present study is described in Sec. II. Gyrokinetic simulation results of the toroidal ITG and self-generated zonal flows during the ITB formation under typical parameters in HL-2A ITB plasmas are presented in Sec. III, where the zonal flow dynamics, wavenumber spectra of turbulent entropy production, and ion thermal transport have been analyzed. Finally, concluding remarks and discussions are given in Sec. IV.

## II. SIMULATION MODEL

In this section, the gyrokinetic simulation model and entropy balance relations considering microinstabilities and turbulence in magnetically confined toroidal plasmas are presented, which are limited to the local approximations. In addition, the numerical settings are explained here.

### A. Entropy balance diagnostics

For gyrokinetic or gyrofluid turbulence simulations, one of the choices is to analyze the nonlinear behaviors of low-order moments of the velocity-space distribution function  $f$  (fluid variables, such as density, fluid velocity, temperature, and so on). However, it is noteworthy that the fluid variables cannot describe fine-scale fluctuations of  $f$  generated by the phase mixing. This is related to the fact that the transport flux itself is described by correlations between these low-order moments and electromagnetic fields. Another choice is a quasisteady state with a mean transport flux, for example, the ITG turbulence with adiabatic electrons will reach the quasisteady state with  $d\delta S/dt = \eta_i Q_i \neq 0$  and  $dW/dt = 0$ , where  $\delta S$ ,  $Q_i$ , and  $W$  are the entropy variable, ion thermal flux, and potential energy, respectively. In this state, continuous growth of fine-scale structures of  $\delta f$  in the velocity space (high-order moments of  $f$ ) through phase mixing contributes to monotonical increase in the entropy variable associated with fluctuations, while the low-order moments giving  $W$  and  $Q_i$  are constant in average. The quasisteady state is regarded as an idealization of the real steady state where the high-order moments saturate as well due to collisional dissipation, which is more relevant to compare with the anomalous transport observed in experiments.<sup>34</sup> Entropy production occurs to compensate for the negative supply due to the nature of the zero time derivative in the quasisteady state. More importantly, highly confined plasmas with external and/or internal transport barriers have larger negative entropy input. This implies that the confinement performance can be evaluated by the entropy generated by the system.

In this paper, we have employed the gyrokinetic Vlasov turbulence code GKV+,<sup>35–37</sup> which has been widely used in the analyses of microinstabilities in magnetically confined plasmas. In the GKV+ code, a flux tube  $\hat{s}$ - $\alpha$  equilibrium model<sup>38</sup> is employed with the field-aligned coordinates: the radial coordinate  $x = \rho - \rho_0$ , the field-line label  $y = a[\rho_0/q(\rho_0)][q(\rho)\theta - \zeta]$ , the parallel coordinate  $z = \theta$ , where  $a$ ,  $\rho$ ,  $\theta$ ,  $\zeta$ , and  $q$  are the plasma minor radius, flux surface label, poloidal and toroidal angles, and the safety factor, respectively. The gyrocenter distribution function for a species  $s$  is divided into the Maxwellian and the perturbed parts  $F_s = F_{Ms} + \tilde{f}_s$  where  $F_{Ms} = \frac{n_s}{(2\pi T_s/m_s)^{3/2}} \exp\left(-\frac{m_s v_{\parallel}^2}{2T_s} - \frac{\mu B}{T_s}\right)$ . The velocity and magnetic moment

are defined as  $\mathbf{v} = v_{\parallel}\mathbf{B}/B + \mathbf{v}_{\perp}$  and  $\mu = m_s v_{\perp}^2/(2B)$ , respectively. By taking the flux surface average of the kinetic form of the neoclassical entropy production, the conjugate pairs of the thermodynamic forces and the neoclassical fluxes are rigorously identified from the thermodynamic form, in which the anomalous transport fluxes are clearly identified from the anomalous entropy production rate (see Ref. 39 and references therein). The zero-dimensional entropy balance relation governing the quadratic form of the distribution function can be obtained by summing over all modes and species. In the present study, the electromagnetic effect is neglected as the adiabatic electron response has been assumed; hence, the entropy balance equations are given by

$$\frac{d}{dt} \left( \sum_s \delta S_s + W_{es} \right) = \sum_s \left( \frac{\Theta_s}{L_{T_s}} + D_s \right), \quad (1)$$

$$\delta S_{s\mathbf{k}_{\perp}} = \left\langle \int d^3 v \frac{T_s |\tilde{f}_{s\mathbf{k}_{\perp}}|^2}{2F_{Ms}} \right\rangle,$$

$$D_{s\mathbf{k}_{\perp}} = \left\langle \int d^3 v \frac{T_s}{F_{Ms}} \left( \tilde{f}_{s\mathbf{k}_{\perp}}^* + \frac{q_s}{T_s} \phi_{\mathbf{k}_{\perp}}^* J_0 F_{Ms} \right) C_s(h_{s\mathbf{k}_{\perp}}) \right\rangle, \quad (2)$$

$$W_{es\mathbf{k}_{\perp}} = \left\langle \left( \lambda_{Di}^2 k_{\perp}^2 + \sum_s \frac{q_s^2}{T_s} [1 - \Gamma_0(b_{sk})] \right) \frac{|\phi_{\mathbf{k}_{\perp}}|^2}{2} \right\rangle, \quad (3)$$

$$\Theta_{es,\mathbf{k}_{\perp}} = \left\langle \text{Re} \left[ \left( \frac{1}{2} \tilde{p}_{\parallel s\mathbf{k}_{\perp}} + \tilde{p}_{\perp s\mathbf{k}_{\perp}} - \frac{5}{2} T_s \tilde{n}_{s\mathbf{k}_{\perp}} \right) \left( \frac{-ik_y \phi_{\mathbf{k}_{\perp}}}{B} \right)^* \right] \right\rangle, \quad (4)$$

$$C_s = \nu_s \left[ \frac{\partial}{\partial v_{\parallel}} \left( v_{\parallel} h_{s\mathbf{k}_{\perp}} + v_{Ts}^2 \frac{\partial h_{s\mathbf{k}_{\perp}}}{\partial v_{\parallel}} \right) + \frac{1}{v_{\perp}} \frac{\partial}{\partial v_{\perp}} \right. \\ \left. \times \left( v_{\perp}^2 h_{s\mathbf{k}_{\perp}} + v_{Ts}^2 v_{\perp} \frac{\partial h_{s\mathbf{k}_{\perp}}}{\partial v_{\perp}} \right) \right], \quad (5)$$

where  $\delta S_s = \sum_{\mathbf{k}_{\perp}} \delta S_{s\mathbf{k}_{\perp}}$ ,  $W_{es} = \sum_{\mathbf{k}_{\perp}} W_{es\mathbf{k}_{\perp}}$ ,  $\Theta_{es,s} = \sum_{\mathbf{k}_{\perp}} \Theta_{es,\mathbf{k}_{\perp}}$ , and  $D_s = \sum_{\mathbf{k}_{\perp}} D_{s\mathbf{k}_{\perp}}$ . The  $C_s(h_{s\mathbf{k}_{\perp}})$  is Lenard-Bernstein collision operator where  $h_{s\mathbf{k}_{\perp}} = \tilde{f}_{s\mathbf{k}_{\perp}} + \frac{q_s}{T_s} \phi_{\mathbf{k}_{\perp}} J_0 F_{Ms}$  donates the nonadiabatic part of the gyrocenter distribution function. The notations  $\delta S_{s\mathbf{k}_{\perp}}$ ,  $W_{es\mathbf{k}_{\perp}}$ ,  $D_{s\mathbf{k}_{\perp}}$ , and  $\Theta_{s\mathbf{k}_{\perp}}$  are the perturbed entropy, the electrostatic energy, the collisional dissipation, and heat flux, respectively. The bracket  $\langle \dots \rangle$  and  $*$  denote the flux surface average and the complex conjugate, respectively. The zeroth-order Bessel function is defined as  $J_0 = J_0(k_{\perp} \rho_s)$ .  $\Gamma_0 = e^{-k_{\perp}^2 \rho_s^2} I_0(k_{\perp}^2 \rho_s^2)$  where  $\rho_s$  and  $I_0$  are the Larmor radius and zeroth-order modified Bessel function, respectively. The ion Debye-length and thermal velocities are  $\lambda_{Di} = \sqrt{T_i/4\pi e^2 n_i}$  and  $v_{Ts} = \sqrt{T_s/m_s}$ , respectively. The  $q_s$  and  $\nu_s$  are the charge number and collision for each species, respectively. The notations  $B$  and  $k_y$  are the magnetic field strength and binormal wavenumber, respectively. Temperature gradients are represented by the critical parameter  $\eta_s = L_n/L_{T_s}$  where  $L_n = -(d \ln n/dx)^{-1}$  and  $L_{T_s} = -(d \ln T_s/dx)^{-1}$  are the density and temperature scale lengths, respectively. The perturbed density, parallel component of velocity, and parallel and perpendicular pressures are given by  $\tilde{n}_{s\mathbf{k}_{\perp}} = \int \tilde{f}_{s\mathbf{k}_{\perp}} J_0 d^3 v$ ,  $\tilde{p}_{\parallel s\mathbf{k}_{\perp}} = \int \frac{q_s}{T_s} (1 - \Gamma_0) \phi_{\mathbf{k}_{\perp}} \tilde{u}_{\parallel s\mathbf{k}_{\perp}} d^3 v$ ,  $\tilde{p}_{\parallel s\mathbf{k}_{\perp}} = \int m_s v_{\parallel}^2 \tilde{f}_{s\mathbf{k}_{\perp}} J_0 d^3 v$ , and  $\tilde{p}_{\perp s\mathbf{k}_{\perp}} = \int \mu B \tilde{f}_{s\mathbf{k}_{\perp}} J_0 d^3 v$ , respectively. The normalizations of the coordinates and variables are  $(t v_{Ti}/R_0, \mathbf{k}_{\perp} \rho_i, z, v_{\parallel}/v_{Ti}, \mu B_0/T_s,$

$$\tilde{f}_{s\mathbf{k}_{\perp}} v_{Ts}^3 R_0/n_s \rho_i, \tilde{\phi}_{\mathbf{k}_{\perp}} e R_0/T_i \rho_i, \tilde{A}_{\parallel \mathbf{k}_{\perp}} R_0/B_0 \rho_i^2) \rightarrow (t, \mathbf{k}_{\perp}, z, v_{\parallel}, \mu, \tilde{f}_{s\mathbf{k}_{\perp}}, \tilde{\phi}_{\mathbf{k}_{\perp}}, \tilde{A}_{\parallel \mathbf{k}_{\perp}}).$$

## B. Numerical settings

The equations are numerically solved by using the gyrokinetic Vlasov simulation code GKV+. Finite difference methods with a low-pass filter are employed to discretize the partial derivatives in the field-aligned coordinate and velocity space coordinates. The nonlinear terms are evaluated by means of the Fourier spectral method, which is computationally parallelized with the computation-communication overlap techniques.<sup>40</sup> Time advancement is performed using the fourth-order Runge–Kutta–Gill method. Electrostatic limit is assumed as the plasma beta is low ( $\beta_e < 0.17\%$  in the region of interest) in the present steady-state HL-2A ITB discharges; hence, the turbulence is of electrostatic nature. For the nonlinear simulations, the domain sizes are basically set to be  $-58.82\rho_i \leq x \leq 58.82\rho_i$ ,  $-62.83\rho_i \leq y \leq 62.83\rho_i$ ,  $-\pi \leq z \leq \pi$ ,  $-4v_{Ti} \leq v_{\parallel} \leq 4v_{Ti}$ , and  $0 \leq \mu B_0/T_i \leq 8$ . The resolution for ITG turbulence has employed  $128 \times 64 \times 64 \times 64 \times 16$  grid points in  $(x, y, z, v_{\parallel}, \mu)$  directions. The perpendicular wave numbers are limited to  $(-3 \leq k_x \rho_i \leq 3)$  and  $(-1 \leq k_y \rho_i \leq 1)$  for the present cases, and the 2/3 de-aliasing rule is applied to the Fourier spectral calculation in  $x$  and  $y$  directions. Convergence tests were carried out for representative simulations in this work, during which the nonlinear simulations have demonstrated that the peak value of the heat flux spectrum would show an increase in about  $\sim 10\%$  while the total flux would only become about  $\sim 5\%$  larger when the grid resolutions, box size, and number of radial modes are doubled. The turbulence structure can be well resolved in the simulations as the radial size of the turbulence is around  $10\rho_i$ . In addition, the entropy balance relations and zonal flow structures are converged as well hence the simulation box size and grid resolutions are sufficient in the present study. The artificial diffusion is set to  $10^{-2}$ ; hence, the transport is not largely affected by the hyperviscosity as enough resolution has been applied.

## III. SIMULATION RESULTS

In order to clarify the basic feature of the dependence of ITG mode on the parameters  $\tau$  and  $\eta_b$ , the numerical test for the collisionless electrostatic ITG mode using GKV+ based on the Cyclone base case (CBC) parameter set<sup>41</sup> has been done where the physical parameters are as follows: safety factor  $q = 1.4$ , magnetic shear  $\hat{s} = (r/q)dq/dr = 0.78$ , inverse aspect ratio  $\varepsilon = 0.18$ , and density gradient  $R/L_n = 2.22$ . The normalized poloidal wavenumber is set to  $k_{\theta} \rho_i = 0.2$  as the growth rate peaks around this wavenumber for the CBC parameters in a deuterium plasma. The result shown in Fig. 1 clearly indicates that the ITG is destabilized by  $\eta_b$ , whereas it is stabilized by  $\tau$  when the value of  $\tau$  is larger than unity. It is thus implied that the suppression of ITG turbulence by increasing  $\tau$  is a generic feature in gyrokinetic ITG turbulence, which is also important in the present study of the zonal flow dynamics and ion transport during ITB formation on the HL-2A tokamak, where a significant increase in  $\tau$  is observed in the experiments through neutral beam injection.

### A. Linear stability of ITG during ITB formation

The profiles used in this paper are described here. The basic discharge waveforms of HL-2A shot #25733 deuterium plasma are shown

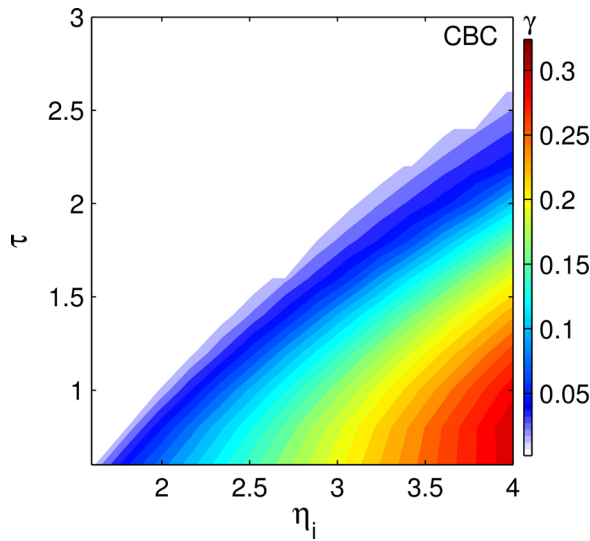


FIG. 1. ITG growth rate as a function of  $\tau$  and  $\eta_i$  for CBC parameters. The growth rate is normalized by  $v_{Ti}/R_0$ .

in Fig. 2, which is a typical ITB discharge.<sup>32</sup> For shot #25733, the barrier forms at time  $t = 537.5$  ms and is well developed at  $t = 550$  ms, as indicated by the vertical dashed lines in Fig. 2(a). The plasma stored energy starts to saturate when the ITB is fully developed, as seen in Fig. 2(b). The plasma shape and flux surfaces shown in Fig. 2(c) are calculated by the equilibrium and reconstruction fitting code (EFIT). It is clearly indicated that plasma equilibrium exhibits a circular geometry and has quite little change during the time of interest. It is noted that the time slice used at the ITB formation is slightly differ from that in Fig. 2(a) due to the fact that the temporal resolution of the EFIT is restricted to 1 ms. However, it is strongly believed that the equilibrium would be basically the same at  $t = 537$  and  $t = 537.5$  ms during the discharge; hence, the simulation results are reliable. The corresponding profiles of safety factor  $q$  and magnetic shear  $\hat{s}$  averaging over the time range 525–550 ms with a time interval of 1 ms are shown in Fig. 2(d), where the small error bars also indicate that the equilibrium has almost no change during the ITB formation.

Shown in Fig. 3 are the profiles of ion temperature  $T_i$ , electron temperature  $T_e$ , and electron density  $n_e$  during the ITB formation. The  $T_i$  is measured with a 32-channel charge exchange recombination spectroscopy (CXRS) diagnostic system with spatial and temporal resolutions about  $\sim 1.5$  cm and 12.5 ms.<sup>42</sup> A 32-channel fast electron cyclotron emission (ECE) system provides the  $T_e$  with temporal and spatial resolutions up to  $0.8 \mu\text{s}$  and 1 cm.<sup>43</sup> It is suggested that there is no ITB at  $t = 525$  ms as  $T_i$  and  $T_e$  are comparable with each other, and the increase in  $T_i$  is mainly contributed from the heating of ions, while the ITB starts to form at  $t = 537.5$  ms due to an obvious increasing of ion temperature gradient and  $T_i/T_e$ . The density profiles  $n_e$  are reconstructed from the formic acid (HCOOH) laser interferometer<sup>44</sup> measurements through Abel inversion method. All of these profiles are mapped on to the flux surface coordinates. It is clearly seen that the  $T_i$  and its gradient have increased significantly during the ITB formation, where the location of the largest gradient and ITB foot are around  $\rho \approx 0.4$  and  $\rho \approx 0.5$ , respectively. The  $T_e$  has also increased slightly as the

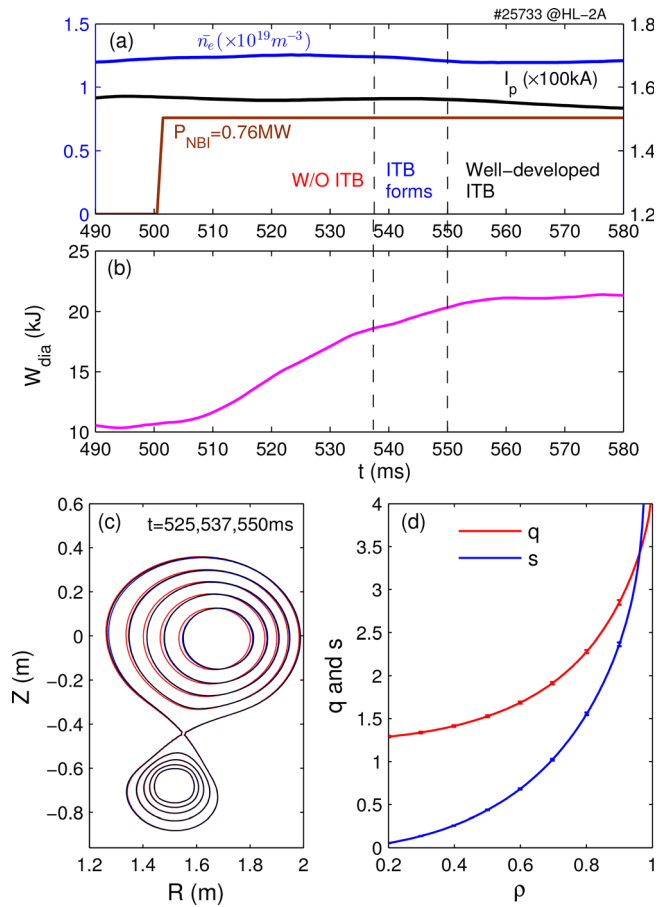


FIG. 2. Waveforms of (a) line-averaged density, plasma current, and NBI heating power, (b) stored energy, (c) flux surfaces, and (d) profiles of safety factor and magnetic shear during typical ITB discharge in HL-2A.

NBI heats electrons and ions at the same time, whereas the  $n_e$  is shown to be slightly decreased during the ITB formation.

As discussed previously, the stability property of ITG depends on both the temperature gradient  $\eta_i$  and ion-to-electron temperature ratio  $\tau$ ; hence, it is meaningful to resolve the regions where the ITG could survive. Figure 4(a) shows the profiles of normalized ion temperature gradient  $R/L_{Ti}$  and density gradient  $R/L_n$ . The  $\eta_i$  and  $\tau$  shown in Figs. 4(b) and 4(c) have demonstrated that both the two parameters have increased during the ITB formation. The maximum  $\eta_i$  occurs at  $\rho \approx 0.4$  for all the three time slices. The theoretical value including the temperature ratio effect<sup>45</sup> that ITG can be destabilized is calculated by  $\eta_{ic}^{th} = \left(\frac{2}{3} - \frac{1}{2\tau} + \frac{R}{8L_n}\right) + \frac{L_n}{R} \left(\frac{1}{2\tau} + \frac{9\tau}{20}\right)$ , as shown by the dashed lines in Fig. 4(a). The  $\eta_i$  is larger than  $\eta_{ic}^{th}$  almost within the region  $0.3 \leq \rho \leq 0.6$ , suggesting that the ITG turbulence mainly exists inside the ITB. The experimental values of  $\eta_i$  is smaller than 1 for  $\rho \geq 0.85$ ; thus, the ITGs cannot be excited at these positions, where it is believed that the TEMs and resistive edge modes are responsible for the turbulent transport.

The dependence of linear stability of ITG mode based on the experimentally deduced  $\eta_i$  and  $\tau$  is shown in Fig. 5. The poloidal

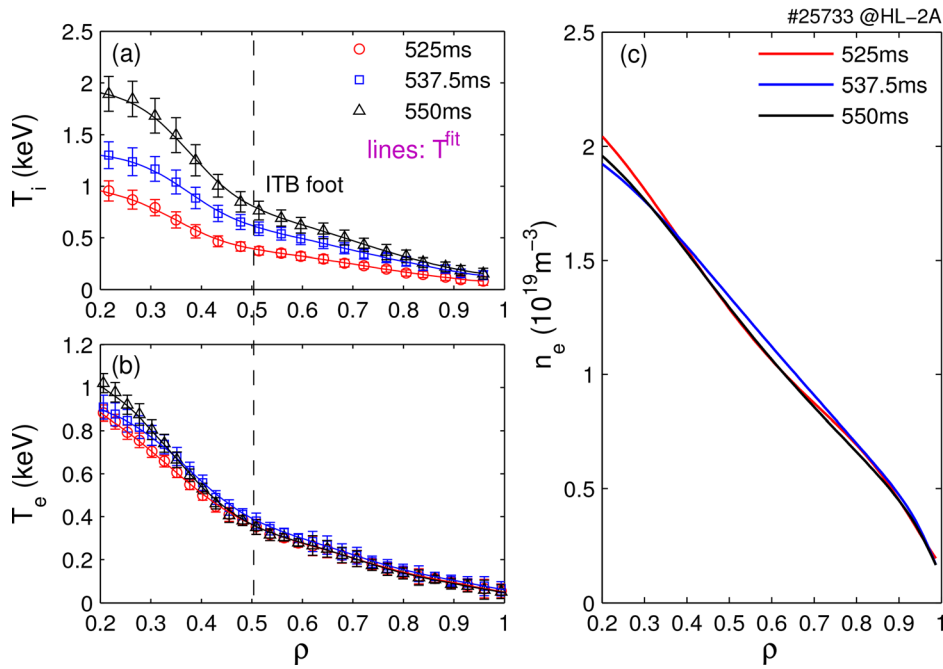


FIG. 3. Radial profiles of (a) ion temperature  $T_i$ , (b) electron temperature  $T_e$ , and (c) Abel inverted electron density  $n_e$  during the ITB formation.

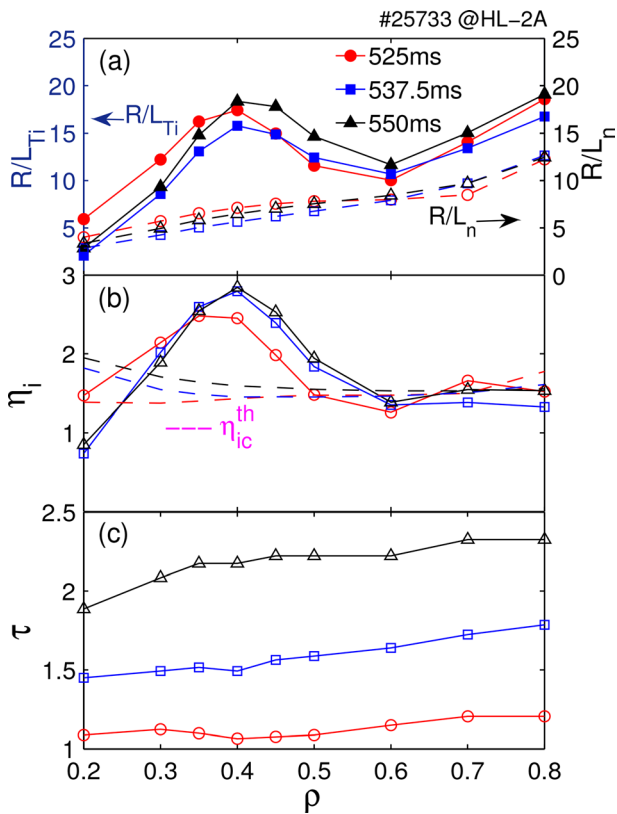


FIG. 4. Profiles of (a) normalized ion temperature gradient  $R/L_{T_i}$  and density gradient  $R/L_n$ , (b) critical parameter  $\eta_i$ , and (c) ion-to-electron temperature ratio  $\tau$  during the ITB formation.

wavenumber is  $k_{\theta}\rho_i = 0.4$  while the other physical parameters are basically set to the values of  $t = 550$  ms at  $\rho = 0.4$ . The horizontal and vertical error bars donate the range of  $\eta_i$  and  $\tau$  calculated from Fig. 4. It is shown that the ITG mode locates almost around the most unstable region of  $\eta_i$  and  $\tau$  at  $t = 525$  ms, and it moves gradually to the upper stability boundary during the ITB formation as the value of  $\tau$  becomes obviously larger whereas the change in the value  $\eta_i$  is un conspicuous. The result is consistent with that in CBC cases as in Fig. 1,

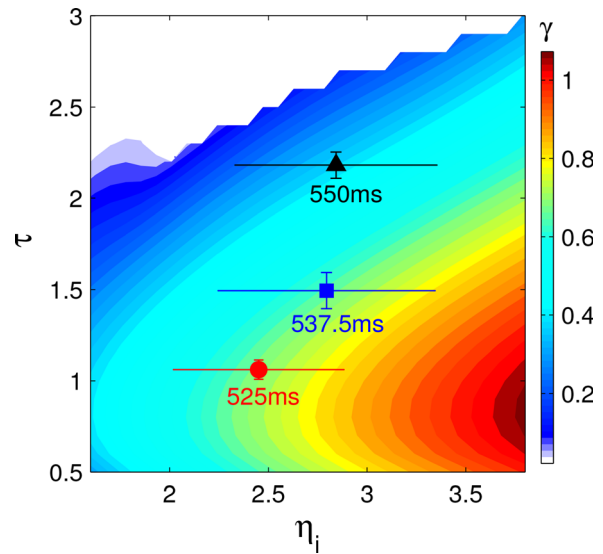


FIG. 5. Dependence of ITG growth rate on  $\tau$  and  $\eta_i$  for the HL-2A ITB discharge. The symbols donate the values deduced from the experimental measurements.

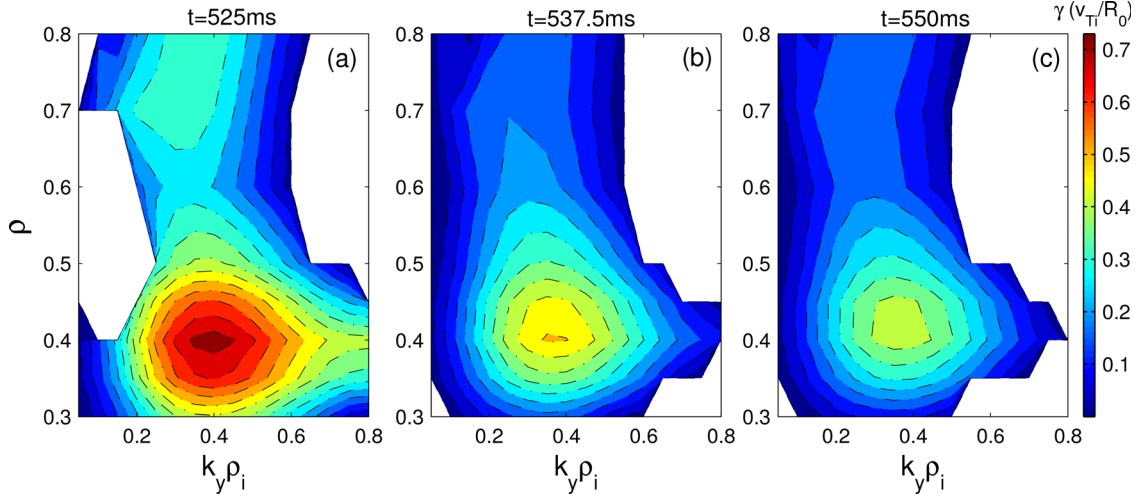


FIG. 6. Normalized growth rate as a function of wavenumber  $k_y \rho_i$  and radial position  $\rho$  during ITB formation: (a) without ITB, (b) when ITB triggers, and (c) with well-developed ITB.

indicating that the characteristic of ITG turbulence in the process of barrier formation on HL-2A can be well described by the interaction and competition between the driving effect of  $\eta_i$  and damping effect of  $\tau$ .

The contour plot depicted in Fig. 6 is the linear stability of ITG mode, where the physical parameters are deduced from the cubic fitting of the experimentally measured values. It is discovered that the maximum growth rate peaks around  $k_y \rho_i \approx 0.4$  and the modes mainly exists in the region  $0.3 \leq \rho \leq 0.6$ . The maximum growth rate of ITG  $\gamma^{\max}$  without ITB in Fig. 6(a) is substantially larger than that with an ITB, although the  $\eta_i$  has increased, as shown in Fig. 6(c), which can be explained by the stabilizing effect of  $\tau$  on the stability property of ITG, which is consistent with the conclusions from Fig. 5.

The  $\gamma^{\max}$  as a function of radial position is illustrated in Fig. 7. The  $\gamma^{\max}$  peaks at  $\rho \approx 0.4$ , corresponding to the position of maximum ion temperature gradient. The growth rate shows an obvious decrease when ITB starts to form, particularly inside the ITB region, while the modes are further slightly stabilized when the ITB has been fully developed. The negative values of real frequency indicate that the modes rotate in the ion diamagnetic direction.

In addition, it is widely known that kinetic electron response would destabilize ITG modes; therefore, it is necessary to evaluate the influence of this effect. We have calculated the eigenvalue spectrum for the case of well-developed ITB accordingly, i.e.,  $t = 550$  ms at  $\rho = 0.4$  with kinetic electron response, as shown by Fig. 8, where both the electron temperature gradient and  $\beta$  are set to zero. It is found that the peak of the growth rate spectrum shifts slightly to lower  $k$  and the maximum value shows an increase in about 9% in comparison with adiabatic electron response. However, it should be noted that the ITG will be stabilized by finite  $\beta$  although the  $\beta$  is low in the discharge. Thus, it can be concluded that the effect of kinetic electron response is expected to be small, which will not change the nature of the turbulence as well as the ZF dynamics, and simulations with adiabatic electron response can capture the basic feature of the turbulence transport for the case of an ion internal transport barrier.

### B. Zonal flow dynamics and turbulent transport during ITB formation

The dynamics of self-generated zonal flows and ITG turbulence during the formation of ITB is carried out by nonlinear gyrokinetic simulations based on the parameters deduced from the experimental values. Time evolutions of each term in the entropy balance relation,

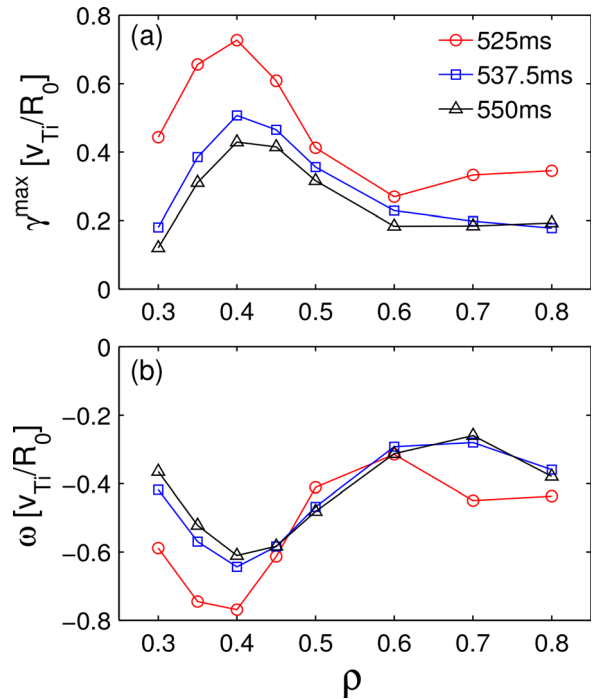
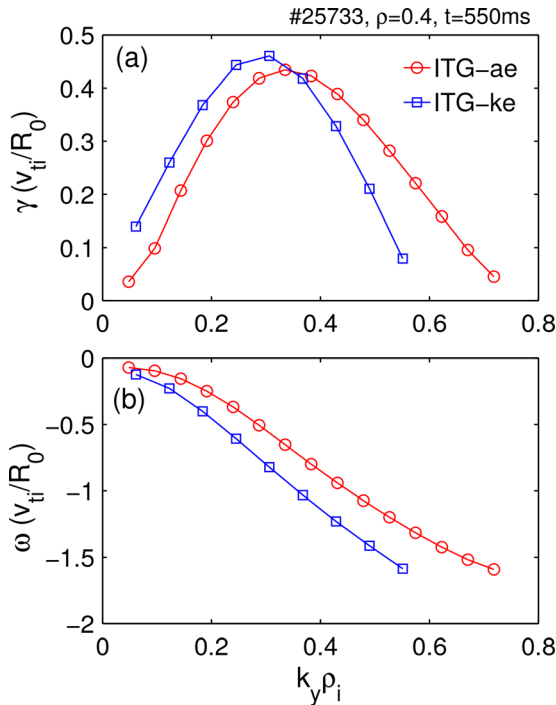


FIG. 7. (a) Maximum growth rate and (b) corresponding real frequency as a function radial position during ITB formation.



**FIG. 8.** Comparison between the wavenumber spectrum of (a) growth rate and (b) real frequency of the ITG with adiabatic electron response (ITG-ae) and kinetic electron response (ITG-ke).

Eq. (1), for the toroidal ITG turbulence without ITB, at the time ITB triggers and with well-developed ITB at radial position  $\rho = 0.4$  are plotted in Figs. 9(a)–9(c), respectively. It has been recognized that the electrostatic flux terms  $\Theta_{iE}/L_{Ti} > 0$  will drive strong ion entropy in ITG turbulence, which is balanced to the ion collisional dissipation  $D_i < 0$  and other terms are subdominant.<sup>35</sup> These characters are clearly discovered in Fig. 6. The ion entropy drive due to flux terms are reduced when ITB is triggered, implying that the ITG turbulence will be reduced once an ITB has been constructed.

The poloidal wavenumber spectrum of ion entropy driven by ion flux terms is depicted in Fig. 10, which is summed over all the radial wavenumbers and averaged during the time range of  $80 \leq tv_{Ti}/R_0 \leq 120$  with a time interval of  $10 tv_{Ti}/R_0$ , since the saturation of ITG turbulence and ZF intensity usually occurs at  $tv_{Ti}/R_0 \sim 70$  in the present simulations. The results have shown that the ion entropy drive peaks at around  $k_{\theta}\rho_i \approx 0.4$  for all the cases as this mode has the maximum growth rate. The entropy drive is strongly weakened across the whole spectrum when ITB starts to form, while it is further slightly reduced with a well-developed ITB. Similarly, the entropy drive by radial wavenumber modes integrated over the poloidal wavenumber space is also deduced, as can be seen in Fig. 11. The entropy drive also decreases once the ITB occurs and the deduction of entropy drive at  $\rho = 0.35$  is stronger than that at  $\rho = 0.4$  and  $\rho = 0.45$ . This is identified to be due to the elongated mode structure along the field line at weaker magnetic shear that produces nonlinear self-interactions and may contribute the supplemental reduction of turbulence, which is also in qualitatively consistent with recent simulations showing finite- $\beta$

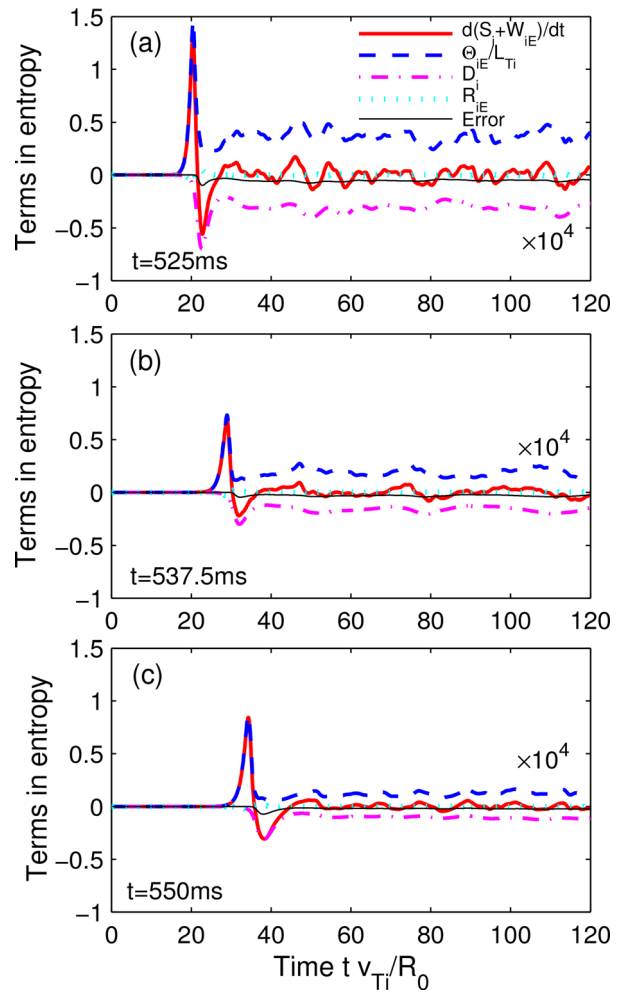


**FIG. 9.** Time evolution of the dominant terms in the entropy balance in ITG turbulence at the time slices of (a) without ITB, (b) ITB triggers, and (c) with well-developed ITB. The terms are normalized by  $n_0 T_i v_{Ti} \rho_i^2 / R_0^3$ .

stabilization becomes significant as magnetic shear decreases.<sup>46</sup> Moreover, it is interesting that the reduction of drive mainly comes from the small and medium radial wavenumbers, i.e.,  $k_x \rho_i < 1.5$ . Another important feature is that the spectrum has been changed in the presence of ITB, that is, spectrum without ITB is characterized by a peak around  $k_x \rho_i = 0.5$ , whereas it shows a smooth decay in the spectrum when ITB is triggered. These results have suggested that not only the ion transport by large-scale turbulence has decreased, but also the strong reduction of heat flux induced by the medium radial wavenumbers during the formation of internal transport barriers.

The well-known saturation mechanism of the ITG turbulence is due to the nonlinearly self-generated zonal flow in fully developed turbulence regime, which would in turn suppress the turbulence through the ZF shearing effect. The structures of electrostatic potential for the three relevant time slices are shown in Fig. 12. It is clearly indicated that the long-range correlation without ITB is relatively weak and do not show an uniform structure along the field line, leading to a small

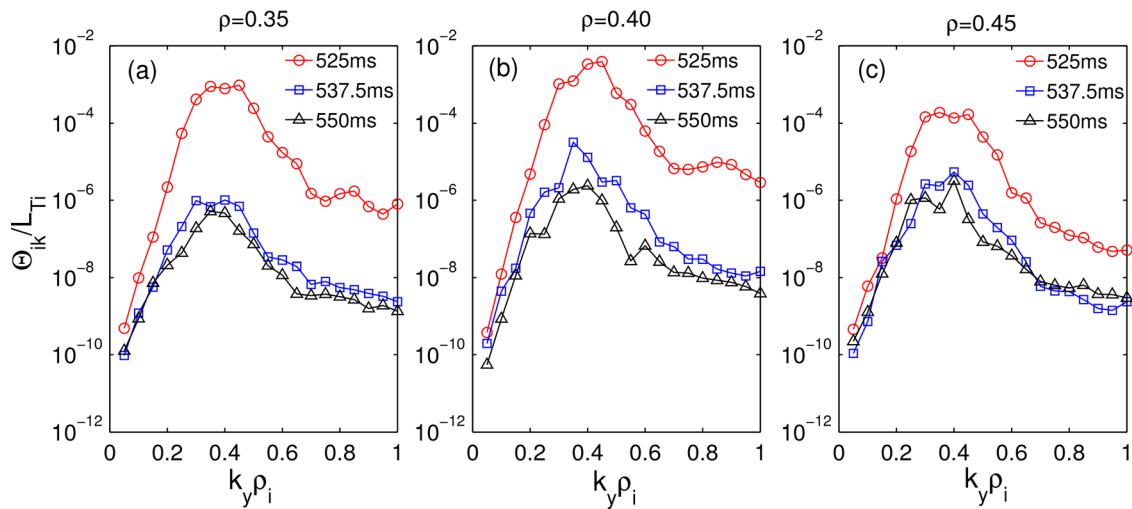


FIG. 10. Poloidal wavenumber spectra of ion entropy drive at (a)  $\rho = 0.35$ , (b)  $\rho = 0.4$ , and (c)  $\rho = 0.45$  during ITB formation.

value of ZF shearing rate  $\omega_{E \times B}^{ZF}$ , which can be concluded from Figs. 12(a1)–12(a3). The ZF intensity is enhanced when ITB forms, especially in the inner region of ITB, as can be found in Figs. 12(b1)–12(b3). A much stronger ZFs compared to the former time slices are discovered at all the positions with a well-developed ITB, showing the features of a long-range correlation along the field line and a large shearing in the radial direction, as seen in Figs. 12(c1)–12(c3). In this case, the large radial scale turbulent structures are torn apart and scattered to higher wave-numbers domain, hence reducing the ion heat transport and being beneficial to the confinement.

The radial profile of the relative energy of ZFs and turbulence is illustrated in Fig. 13. Clearly seen in the figure is that the ZF energy has increased across the whole plasma region together with the reduction of turbulent energy, indicating that the nonlinear energy transfer

from turbulence to ZF is enhanced thus the turbulent transport will be decreased as the ZFs do not cause transport. In addition, it is found that the ZF energy has clearly become larger for the region of  $\rho > 0.4$  when ITB starts to form, whereas it is significantly increased inside the ITB for the case of a fully developed ITB. This result has implied that the transport during the ITB formation is consisted by two processes: first, the reduction of ion transport and the increase in ZF are mainly contributed from the outer region  $\rho > 0.4$  as ITB is triggered; second, the ZF inside the ITB will be enhanced remarkably while it also further increases outside the ITB when the barrier is well developed, hence leading to the enhancement of confinement across the whole plasma region during the ITB formation.

From the discussions above, the reduction of ion heat transport is a result of the enhancement of the zonal flow shearing rate, which is

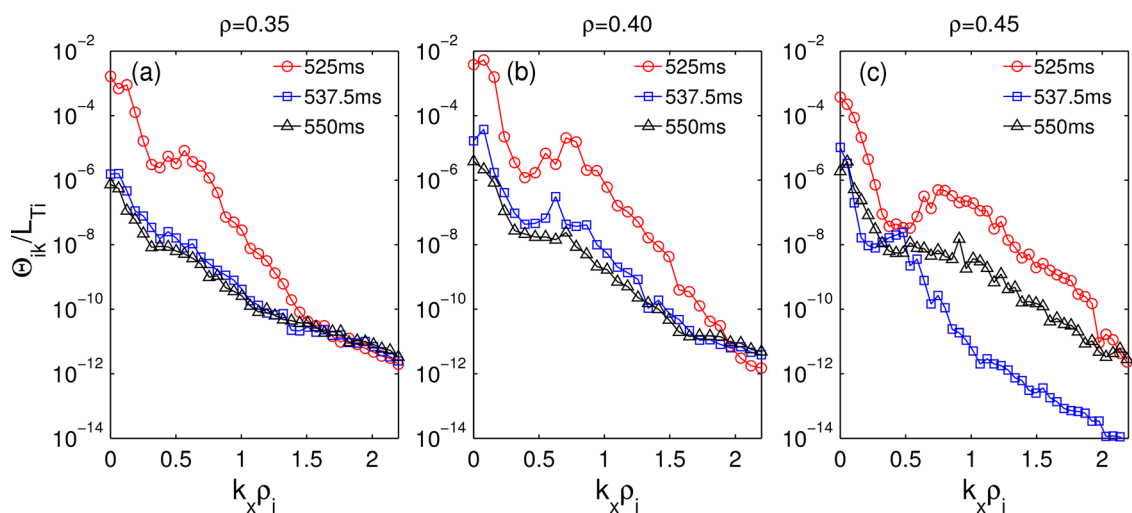
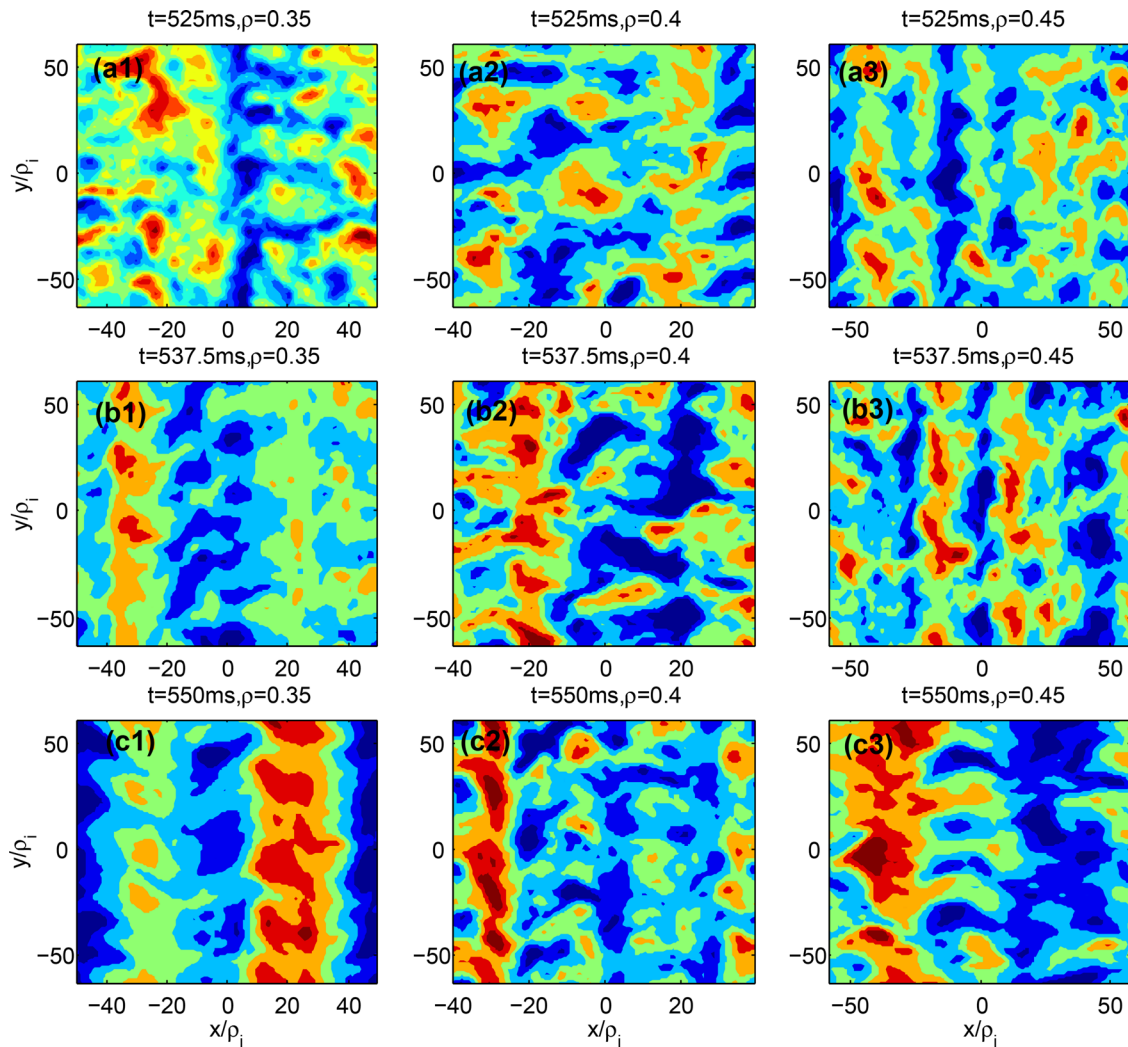


FIG. 11. Radial wavenumber spectra of ion entropy drive at (a)  $\rho = 0.35$ , (b)  $\rho = 0.4$ , and (c)  $\rho = 0.45$  during ITB formation.



**FIG. 12.** Spatial structure of electrostatic potential at three radial positions  $\rho = 0.35, 0.4,$  and  $0.45$  during the ITB formation. (a1)–(a3) are the ZF structures without ITB, while (b1)–(b3) and (c1)–(c3) are that for the time slices when ITB is triggered and with a well-developed ITB, respectively.

defined as  $\omega_{E \times B}^{ZF} = (r/q)\partial(E_r^{ZF}/RB_0)/\partial r$ . The corresponding shearing rate and ion heat transport coefficient are shown in Figs. 14(a) and 14(b), respectively, where the values are averaged in the time range of  $80 \leq tv_{Ti}/R_0 \leq 120$  with temporal resolutions of  $1 tv_{Ti}/R_0$  and  $0.1 tv_{Ti}/R_0$ , respectively. Compared with the results of the linear stability, the ZF shearing rate is slightly increased when ITB forms, but a relatively large  $\omega_{E \times B}^{ZF}$  is realized as the ITB is fully developed particularly inside the ITB region, which can be seen in Fig. 14(a). The ion heat flux shows a strong reduction when ITB is triggered and further decreases when ITB is well-developed, as depicted by Fig. 14(b). It is in qualitative agreement with the heat flux deduced by experimental power balance technique using One Modeling Framework for Integrated Tasks (OMFIT), as shown by the insert. The discrepancy between simulations and experiments may come from several reasons, such as electromagnetic stabilization and mean  $\mathbf{E} \times \mathbf{B}$  shearing. However, it is proved that the ZF shearing rate is of an order magnitude

larger than the global electric field shearing rate which is determined by the toroidal rotation,  $\gamma_E = \rho/q\partial\Omega_{tor}/\partial\rho \sim 0.04 - 0.07$  ( $\rho = 0.4$ ), where  $\Omega_{tor}$  is the toroidal angular velocity. In the experiments, the rotation is relatively low, implying that the suppressing effect resulted from the global electric field can be neglected; hence, it could be concluded that the reduction of ion heat transport is ascribed to the enhancement of zonal flows rather than the global electric field shearing. This result suggests that even a small increase in the amplitude of ZF and its shear has significant suppressing effect on the heat transport. The heat transport coefficient has decreased by a factor of about 3 comparing the cases of with and without transport barriers, as shown in Fig. 14(c).

Based on the analysis of the linear stability and dynamics of the nonlinearly self-generated zonal flows, the possible physical mechanism behind the suppression of ITG turbulence could be explained as follows: the ITG is destabilized by the increasing of  $\eta_i$  whereas it is stabilized by an increasing  $\tau$ , namely, the characteristics of the mode is a

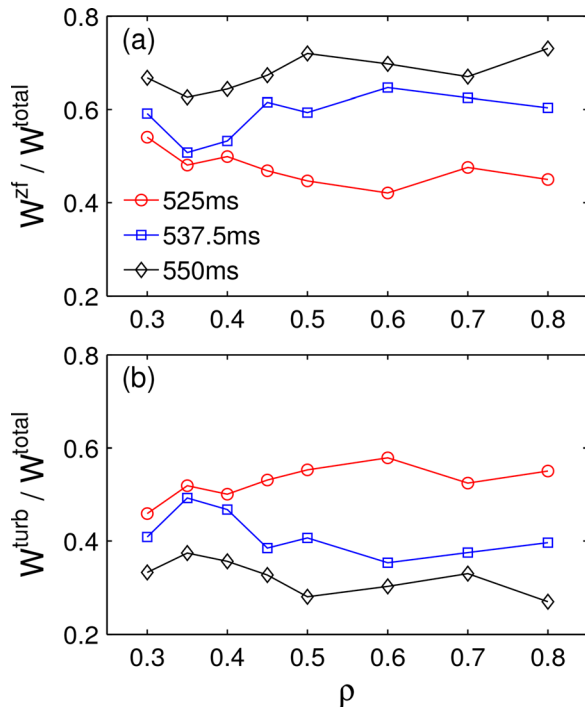


**FIG. 13.** Radial profiles of relative (a) zonal flow energy and (b) turbulent energy during the ITB formation.

results of the combined action and competition between the two effects. Meanwhile, we can expect that if the ZF shearing rate  $\omega_{E \times B}^{ZF}$  is larger than the maximum linear growth rate  $\gamma^{\max}$ , the ITG turbulence will be greatly suppressed.<sup>47</sup> The ratio  $\omega_{E \times B}^{ZF} / \gamma^{\max}$  would approach to unity once the driving effect of  $\eta_i$  is balanced by the damping effect of  $\tau$ ; thus, the ratio of  $\tau / \eta_i$  is an important parameter in determining the linear stability and the ZF shear. Figures 15(a) and 15(b) show the  $\gamma^{\max}$  and  $\omega_{E \times B}^{ZF}$  as a function of  $\tau / \eta_i$  in which the  $\gamma^{\max}$  tends to approach a certain value while the  $\omega_{E \times B}^{ZF}$  shows a continuously increasing in the case of  $\tau / \eta_i > 1.4$ . The value of  $\omega_{E \times B}^{ZF} / \gamma^{\max}$  is shown in Fig. 15(c), which clearly indicates that  $\omega_{E \times B}^{ZF} < \gamma^{\max}$  for most of the positions without ITB. Several values are larger than unity at the beginning of ITB formation, while all of them are larger than unity once the ITB is fully developed, implying that the ITG turbulence can be strongly reduced across the whole plasma region due to the ZF shearing effect and hence the improvement of the confinement. However, it should be noted that the value strongly depends on the detailed physical parameters and magnetic configuration; hence, the systematic investigation is certainly needed in the future.

#### IV. CONCLUSION AND DISCUSSION

In the present study, the linear stabilities, entropy balance relations, and nonlinearly self-generated zonal flows in toroidal ITG turbulence during the ITB formation on the HL-2A tokamak have been examined by means of five-dimensional linear and nonlinear gyrokinetic Vlasov simulation code, GKV+. The maximum growth rate peaks around  $k_\theta \rho_i \approx 0.4$  at  $\rho \approx 0.4$ , and the modes mainly exists inside the ITB region. The ITG turbulence is suppressed in the plasma core

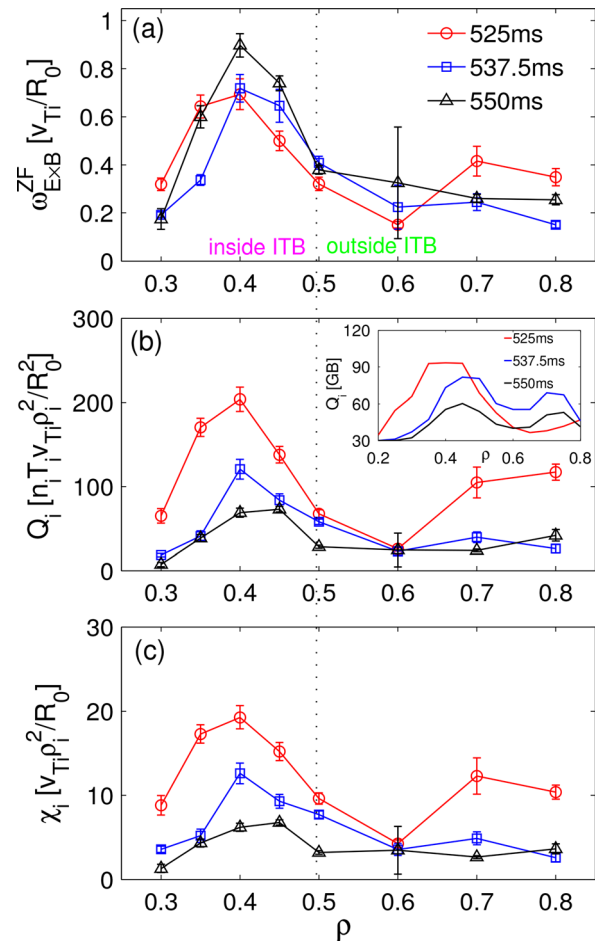


**FIG. 14.** Radial profiles of (a) zonal flow shearing rate  $\omega_{E \times B}^{ZF}$ , (b) ion heat flux  $Q_i$ , and (c) ion heat transport coefficient  $\chi_i$  during the ITB formation. The heat flux (in gyroBohm units) calculated from experimental power balance is shown by the inset.

and in the barrier region at the beginning of barrier formation without recourse to the usual requirements of velocity shear, which can be explained by the stabilizing effect of  $\tau$  on the ITG mode. The entropy balance analyses have shown that the ion entropy drive is strongly reduced for all of the poloidal wavenumbers when ITB is triggered, while it is further reduced slightly with a well-developed ITB. In addition, the radial wavenumber spectrum of the entropy drive has been modified if an ITB exists, i.e., spectrum without ITB is characterized by a peak around  $k_x \rho_i = 0.5$ , whereas it shows a smooth decay when ITB forms, implying that the heat flux induced by the medium radial wavenumbers is largely reduced. A strong ZF in the case of fully developed ITB with a long-range poloidal correlation and a large shearing rate in the radial direction is responsible for the decreasing of ion entropy driven and heat transport. The ZF energy gained from the background turbulence is also shown to increase during the barrier formation. The enhancement of ZF shearing rate and reduction of heat transport are discovered during the ITB formation and the effect of ZF shearing on the transport is shown to act mainly inside the ITB. Further analysis has indicated the parameter  $\tau / \eta_i$  plays an important

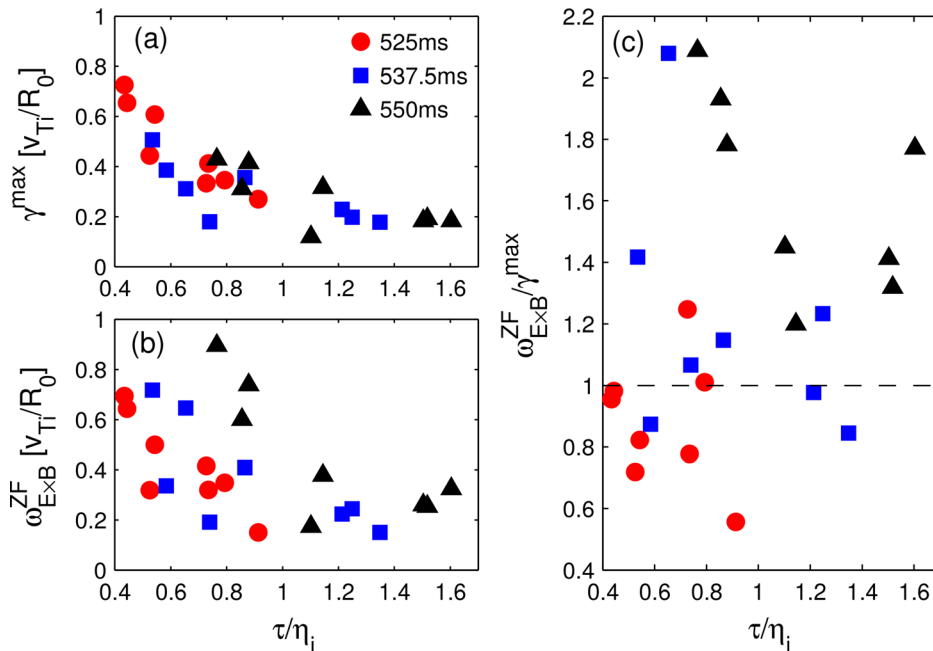


**FIG. 15.** (a) Maximum linear growth rate, (b) zonal flow shearing rate, and (c) the ratio between the former two as a function of  $\tau/\eta_i$ .

role in determining the linear ITG growth rate and ZF shearing rate, whose ratio becomes larger than unity at a certain value of  $\tau/\eta_i$ , and the heat transport driven by ITG turbulence will be greatly suppressed, which is believed to be responsible for the mechanism of ITB formation in the present-day ITB experiments through the method of NBI heating.

The turbulence diagnostics based on entropy production presented here can provide a more systematic method to quantify the effect of the nonlinear interaction on turbulent transport processes. For the nonlinear gyrokinetic plasma turbulence, it is necessary to examine the entropy transfer by means of the entropy balance equation describing explicitly the balance relation among the microscopic fluctuations of the distribution function, the turbulent transport flux, and the collisional dissipation, which allows defining the thermodynamical forces rigorously and gives some insight on the order of magnitude of the various terms. Although the present findings are shown to be beneficial for the understanding of the effect of zonal flows in ITG turbulence during the ITB formation, there are still some important issues that need to be taken into account, for example, the nonlinear electromagnetic stabilization of ITG turbulence and the suppressing effect by global  $\mathbf{E} \times \mathbf{B}$  shear (determined by the toroidal rotation). In addition, the simulations are performed by local approximation as the dimensionless parameter measuring the system size  $1/\rho^* = a/\rho_s$  ( $a$  is the tokamak minor radius and  $\rho_s = \sqrt{T_e/m_i}$  is the ion sound Larmor radius, respectively) is relatively large in ITB discharges on HL-2A, i.e.,  $1/\rho^* > 250$ . However, it is necessary to point out that the system size effect may also have nonnegligible impact on gyrokinetic turbulence, especially for the case of high temperature plasmas.<sup>48,49</sup> Further global gyrokinetic simulations considering the above effects will be carried out to identify the trigger mechanisms and to make quantitative comparison with experimental measurements for the ITB in HL-2A.

## ACKNOWLEDGMENTS

One of the authors J.Q.X. is grateful to Dr. S. Maeyama at Nagoya University for helpful discussions. The authors would like to thank the members of the HL-2A team for operating the device and providing the plasma parameters. We acknowledge the Center for Computational Science and Engineering of Southern University of Science and Technology for providing computational resources. This work was partly supported by the National Key R&D Program of China under Grant Nos. 2019YFE03020000, 2017YFE0300405, 2017YFE0301200 and the National Natural Science Foundation of China (NSFC) under Grant Nos. 12075079, 12005052, 11875019, 11775067, and 11775069.

## AUTHOR DECLARATIONS

### Conflict of Interest

The authors have no conflicts of interest to disclose.

## DATA AVAILABILITY

The data that support the findings of this study are available from the corresponding author upon reasonable request.

## REFERENCES

- <sup>1</sup>E. J. Doyle, W. A. Houlberg, Y. Kamada, V. Mukhovatov, T. H. Osborne, A. Polevoi, G. Bateman, J. W. Connor, J. G. Cordey, T. Fujita, X. Garbet, T. S. Hahm, L. D. Horton, A. E. Hubbard, F. Imbeaux, F. Jenko, J. E. Kinsey, Y. Kishimoto, J. Li, T. C. Luce, Y. Martin, M. Ossipenko, V. Parail, A. Peeters, T. L. Rhodes, J. E. Rice, C. M. Roach, V. Rozhansky, F. Ryter, G. Saibene, R. Sartori, A. C. C. Sips, J. A. Snipes, M. Sugihara, E. J. Synakowski, H. Takenaga, T. Takizuka, K. Thomsen, M. R. Wade, H. R. Wilson, ITPA Transport Physics Topical Group, ITPA Confinement Database, Modelling Topical Group, and ITPA Pedestal and Edge Topical Group, *Nucl. Fusion* **47**, S18 (2007).
- <sup>2</sup>W. Horton, *Rev. Mod. Phys.* **71**, 735 (1999).

- <sup>3</sup>S. E. Parker, W. W. Lee, and R. A. Santoro, *Phys. Rev. Lett.* **71**, 2042 (1993).
- <sup>4</sup>Y. Xiao and Z. Lin, *Phys. Rev. Lett.* **103**, 085004 (2009).
- <sup>5</sup>W. Dorland, F. Jenko, M. Kotschenreuther, and B. N. Rogers, *Phys. Rev. Lett.* **85**, 5579 (2000).
- <sup>6</sup>K. H. Burrell, *Phys. Plasmas* **4**, 1499 (1997).
- <sup>7</sup>P. Maget, X. Garbet, A. Géraud, and E. Joffrin, *Nucl. Fusion* **39**, 949 (1999).
- <sup>8</sup>M. A. Beer, G. W. Hammett, G. Rewoldt, E. J. Synakowski, M. C. Zarnstorff, and W. Dorland, *Phys. Plasmas* **4**, 1792 (1997).
- <sup>9</sup>F. Romanelli, *Phys. Fluids B* **1**, 1018 (1989).
- <sup>10</sup>R. R. Dominguez and G. M. Staebler, *Nucl. Fusion* **33**, 51 (1993).
- <sup>11</sup>F. Wagner, G. Becker, K. Behringer, D. Campbell, A. Eberhagen, W. Engelhardt, G. Fussmann, O. Gehre, J. Gernhardt, G. V. Gierke, G. Haas, M. Huang, F. Karger, M. Keilhacker, O. Klüber, M. Kornherr, K. Lackner, G. Lisitano, G. G. Lister, H. M. Mayer, D. Meisel, E. R. Müller, H. Murmann, H. Niedermeyer, W. Poschenrieder, H. Rapp, H. Röhr, F. Schneider, G. Siller, E. Speth, A. Stäbler, K. H. Steuer, G. Venus, O. Vollmer, and Z. Yü, *Phys. Rev. Lett.* **49**, 1408 (1982).
- <sup>12</sup>R. C. Wolf, *Plasma Phys. Controlled Fusion* **45**, R1 (2003).
- <sup>13</sup>J. W. Connor, T. Fukuda, X. Garbet, C. Gormezano, V. Mukhovatov, M. Wakatani, ITB Database Group, and ITPA Topical Group on Transport Internal Barrier Physics, *Nucl. Fusion* **44**, R1 (2004).
- <sup>14</sup>K. Ida and T. Fujita, *Plasma Phys. Controlled Fusion* **60**, 033001 (2018).
- <sup>15</sup>M. Kotschenreuther, W. Dorland, M. A. Beer, and G. W. Hammett, *Phys. Plasmas* **2**, 2381 (1995).
- <sup>16</sup>G. D. Conway, D. N. Borba, B. Alper, D. V. Bartlett, C. Gormezano, M. G. von Hellermann, A. C. Maas, V. V. Parail, P. Smeulders, and K. D. Zastrow, *Phys. Rev. Lett.* **84**, 1463 (2000).
- <sup>17</sup>T. Fujita, S. Ide, H. Shirai, M. Kikuchi, O. Naito, Y. Koide, S. Takeji, H. Kubo, and S. Ishida, *Phys. Rev. Lett.* **78**, 2377 (1997).
- <sup>18</sup>C. B. Forest, C. C. Petty, M. E. Austin, F. W. Baity, K. H. Burrell, S. C. Chiu, M. S. Chu, J. S. deGrassie, P. Gohil, A. W. Hyatt, H. Ikezi, E. A. Lazarus, M. Murakami, R. I. Pinsky, M. Porkolab, R. Prater, B. W. Rice, G. M. Staebler, E. J. Strait, and T. S. Taylor, *Phys. Rev. Lett.* **77**, 3141 (1996).
- <sup>19</sup>K. Ida, H. Lee, K. Nagaoka, M. Osakabe, C. Suzuki, M. Yoshinuma, R. Seki, M. Yokoyama, T. Akiyama, and LHD Experiment Group, *Phys. Rev. Lett.* **111**, 055001 (2013).
- <sup>20</sup>K. Ida, Y. Sakamoto, M. Yoshinuma, H. Takenaga, K. Nagaoka, N. Hayashi, N. Oyama, M. Osakabe, M. Yokoyama, H. Funaba, N. Tamura, K. Tanaka, Y. Takeiri, K. Ikeda, K. Tsumori, O. Kaneko, K. Itoh, S. Inagaki, T. Kobuchi, A. Isayama, T. Suzuki, T. Fujita, G. Matsunaga, K. Shinohara, Y. Koide, M. Yoshida, S. Ide, and Y. Kamada, *Nucl. Fusion* **49**, 095024 (2009).
- <sup>21</sup>U. Stroth, K. Itoh, S. I. Itoh, H. Hartfuss, H. Laqua, ECRH Team, and WAS Team, *Phys. Rev. Lett.* **86**, 5910 (2001).
- <sup>22</sup>R. Lorenzini, F. Auriemma, A. Fassina, E. Martines, D. Terranova, and F. Sattin, *Phys. Rev. Lett.* **116**, 185002 (2016).
- <sup>23</sup>E. J. Synakowski, S. H. Batha, M. A. Beer, M. G. Bell, R. E. Bell, R. V. Budny, C. E. Bush, P. C. Efthimion, G. W. Hammett, T. S. Hahm, B. LeBlanc, F. Levinton, E. Mazzucato, H. Park, A. T. Ramsey, G. Rewoldt, S. D. Scott, G. Schmidt, W. M. Tang, G. Taylor, and M. C. Zarnstorff, *Phys. Rev. Lett.* **78**, 2972 (1997).
- <sup>24</sup>T. J. J. Tala, J. A. Heikkinen, V. V. Parail, Y. F. Baranov, and S. J. Karttunen, *Plasma Phys. Controlled Fusion* **43**, 507 (2001).
- <sup>25</sup>E. J. Doyle, C. M. Greenfield, M. E. Austin, L. R. Baylor, K. H. Burrell, T. A. Casper, J. C. DeBoo, D. R. Ernst, C. Fenzi, P. Gohil, R. J. Groebner, W. W. Heidbrink, G. L. Jackson, T. C. Jernigan, J. E. Kinsey, L. L. Lao, M. Makowski, G. R. McKee, M. Murakami, W. A. Peebles, M. Porkolab, R. Prater, C. L. Rettig, T. L. Rhodes, J. C. Rost, G. M. Staebler, B. W. Stallard, E. J. Strait, E. J. Synakowski, D. M. Thomas, M. R. Wade, R. E. Waltz, and L. Zeng, *Nucl. Fusion* **42**, 333 (2002).
- <sup>26</sup>Y. Sakamoto, T. Suzuki, S. Ide, Y. Koide, H. Takenaga, Y. Kamada, T. Fujita, T. Fukuda, T. Takizuka, H. Shirai, N. Oyama, Y. Miura, J. T. Team, K. W. Hill, and G. Rewoldt, *Nucl. Fusion* **44**, 876 (2004).
- <sup>27</sup>P. Gohil, J. Kinsey, V. Parail, X. Litaudon, T. Fukuda, T. Hoang, J. W. Connor, E. J. Doyle, Yu. Esipchuk, T. Fujita, S. Lebedev, V. Mukhovatov, J. Rice, E. Synakowski, K. Toi, B. Unterberg, V. Vershkov, M. Wakatani, J. Weiland, T. Aniel, Y. F. Baranov, E. Barbato, A. B. Coulet, C. Bourdelle, G. Bracco, R. V. Budny, P. Buratti, L. Ericsson, B. Esposito, C. Greenfield, M. Greenwald, T. Hahm, T. Hellsten, D. Hogeweij, S. Ide, F. Imbeaux, Y. Kamada, N. Kirneva, P. Maget, A. Peeters, K. Razumova, F. Ryter, Y. Sakamoto, H. Shirai, G. Sips, T. Suzuki, and T. Takizuka, *Nucl. Fusion* **43**, 708 (2003).
- <sup>28</sup>P. H. Diamond, Y. M. Liang, B. A. Carreras, and P. W. Terry, *Phys. Rev. Lett.* **72**, 2565 (1994).
- <sup>29</sup>P. W. Terry, *Rev. Mod. Phys.* **72**, 109 (2000).
- <sup>30</sup>P. H. Diamond, S.-I. Itoh, K. Itoh, and T. S. Hahm, *Plasma Phys. Controlled Fusion* **47**, R35 (2005).
- <sup>31</sup>A. Fujisawa, K. Itoh, H. Iguchi, K. Matsuoka, S. Okamura, A. Shimizu, T. Minami, Y. Yoshimura, K. Nagaoka, C. Takahashi, M. Kojima, H. Nakano, S. Ohsima, S. Nishimura, M. Isobe, C. Suzuki, T. Akiyama, K. Ida, K. Toi, S. I. Itoh, and P. H. Diamond, *Phys. Rev. Lett.* **93**, 165002 (2004).
- <sup>32</sup>D. L. Yu, Y. L. Wei, L. Liu, J. Q. Dong, K. Ida, K. Itoh, A. P. Sun, J. Y. Cao, Z. B. Shi, Z. X. Wang, Y. Xiao, B. S. Yuan, H. R. Du, X. X. He, W. J. Chen, Q. Ma, S. I. Itoh, K. J. Zhao, Y. Zhou, J. Wang, X. Q. Ji, W. L. Zhong, Y. G. Li, J. M. Gao, W. Deng, Y. Liu, Y. Xu, L. W. Yan, Q. W. Yang, X. T. Ding, X. R. Duan, Y. Liu, and HL-2A Team, *Nucl. Fusion* **56**, 056003 (2016).
- <sup>33</sup>Z. H. Qin, K. Imadera, J. Q. Li, and Y. Kishimoto, *Plasma Fusion Res.* **13**, 3403083 (2018).
- <sup>34</sup>J. A. Krommes and G. Hu, *Phys. Plasmas* **1**, 3211 (1994).
- <sup>35</sup>T.-H. Watanabe and H. Sugama, *Nucl. Fusion* **46**, 24 (2006).
- <sup>36</sup>T.-H. Watanabe, H. Sugama, and S. Ferrando-Margalet, *Nucl. Fusion* **47**, 1383 (2007).
- <sup>37</sup>T.-H. Watanabe, H. Sugama, and S. Ferrando-Margalet, *Phys. Rev. Lett.* **100**, 195002 (2008).
- <sup>38</sup>M. A. Beer, S. C. Cowley, and G. W. Hammett, *Phys. Plasmas* **2**, 2687 (1995).
- <sup>39</sup>H. Sugama and W. Horton, *Phys. Plasmas* **4**, 405 (1997).
- <sup>40</sup>S. Maeyama, A. Ishizawa, T. H. Watanabe, N. Nakajima, S. Tsuji-Iio, and H. Tsutsui, *Comput. Phys. Commun.* **184**, 2462 (2013).
- <sup>41</sup>A. M. Dimits, G. Bateman, M. A. Beer, B. I. Cohen, W. Dorland, G. W. Hammett, C. Kim, J. E. Kinsey, M. Kotschenreuther, A. H. Kritiz, L. L. Lao, J. Mandrekas, W. M. Nevins, S. E. Parker, A. J. Redd, D. E. Shumaker, R. Sydora, and J. Weiland, *Phys. Plasmas* **7**, 969 (2000).
- <sup>42</sup>D. L. Yu, Y. L. Wei, L. Liu, J. Y. Cao, Q. Ma, W. J. Chen, Y. Liu, L. W. Yan, Q. W. Yang, and X. R. Duan, *Rev. Sci. Instrum.* **85**, 11E402 (2014).
- <sup>43</sup>Z. B. Shi, M. Jiang, X. L. Huang, W. L. Zhong, W. Chen, Y. L. Che, Z. T. Liu, X. T. Ding, Q. W. Yang, and X. R. Duan, *Rev. Sci. Instrum.* **85**, 023510 (2014).
- <sup>44</sup>Y. G. Li, Y. Zhou, Y. Li, Z. C. Deng, H. X. Wang, and J. Yi, *Rev. Sci. Instrum.* **88**, 083508 (2017).
- <sup>45</sup>A. Casati, C. Bourdelle, X. Garbet, and F. Imbeaux, *Phys. Plasmas* **15**, 042310 (2008).
- <sup>46</sup>A. Ishizawa, D. Urano, Y. Nakamura, S. Maeyama, and T.-H. Watanabe, *Phys. Rev. Lett.* **123**, 025003 (2019).
- <sup>47</sup>H. Biglari, P. H. Diamond, and P. W. Terry, *Phys. Fluids B* **2**, 1 (1990).
- <sup>48</sup>Z. Lin, S. Ethier, T. S. Hahm, and W. M. Tang, *Phys. Rev. Lett.* **88**, 195004 (2002).
- <sup>49</sup>B. F. McMillan, X. Lapillonne, S. Brunner, L. Villard, S. Jolliet, A. Bottino, T. Görler, and F. Jenko, *Phys. Rev. Lett.* **105**, 155001 (2010).